AIP | Journal of Applied Physics

Instability of electrowetting on a dielectric substrate

Jonghyun Park, Xi-Qiao Feng, and Wei Lu

Citation: J. Appl. Phys. **109**, 034309 (2011); doi: 10.1063/1.3544460
View online: http://dx.doi.org/10.1063/1.3544460
View Table of Contents: http://jap.aip.org/resource/1/JAPIAU/v109/i3
Published by the AIP Publishing LLC.

Instability of electrowetting on a dielectric substrate

Jonghyun Park,[1] Xi-Qiao Feng,[2] and Wei Lu[1,a)]
[1]*Department of Mechanical Engineering, University of Michigan, Ann Arbor, Michigan 48109, USA*
[2]*Department of Engineering Mechanics, Tsinghua University, Beijing 100084, China*

(Received 15 September 2010; accepted 11 December 2010; published online 7 February 2011)

The wetting angle of a liquid droplet on a dielectric substrate can be tuned by an applied electric field. Recent experiments revealed an intriguing phenomenon where the contact line between a droplet and a substrate may lose stability under a relatively large field, leading to the ejection of small droplets from the edge of the mother droplet. While this behavior may pose a limit on the achievable wetting angle, it also provides an interesting approach to produce patterns of tiny droplets. We propose a phase field model to explain the mechanism, which combines thermodynamics and convective viscous flow. Our study suggests that instability is preceded by a contact angle reduction and extrusion of a thin layer from the edge of the droplet. While instability appears when the electric field is above a critical value, it can be suppressed with increased surface energy of the droplet. © *2011 American Institute of Physics*. [doi:10.1063/1.3544460]

I. INTRODUCTION

Miniaturization has been a continuing trend in technology because it may bring inherent advantages such as lower cost, higher speed, and greater density. The "lab-on-chip" system for biomedical diagnosis[1,2] is one example fueled by the above advantages. Fully exploring the potential requires controlled surface morphology[3] and morphological transition[4] at small scale. Studies suggest that the wettability of a liquid droplet on a dielectric substrate can be controlled by applying an electric field. This electrowetting approach has become a very promising mechanism to control the surface morphology. Generally speaking, the electrowetting phenomena can be classified into three classes, where an electric field is applied to (i) a conductive droplet, (ii) a dielectric liquid, or (iii) a leaky dielectric liquid. They all have significant potentials for various applications. For instance, in class (i) the controlled electrowetting of conductive droplets has be explored for next generation optical systems such as camera lens,[5–7] where a variable focal length can be achieved by an electric field. Recently Hayes *et al.*[8] proposed an electrowetting-based reflective display technology corresponding to class (ii). In this application an oil film in each pixel ruptures upon the applied voltage and contracts into a corner, which exposes the underlying reflective surface. Another example in this class is electric field induced interface instability of liquid bilayers.[9–13] Based on these effects wetting-dewetting ratchets have been proposed to transport dielectric liquids.[14,15] A leaky dielectric system in class (iii) exploits both the dielectric and conductivity effects.[16]

This paper focuses on controlled electrowetting of conductive droplets, i.e., class (i). The first observation of electrowetting can be traced back to the work of Lippmann,[17] who found that the capillary depression of mercury in contact with electrolyte solutions could be varied by applying an electric field. While conductive water with added ions can demonstrate similar behavior, the electrolytic decomposition of water under the associated current has practically limited the application. Recently several researchers have used thin insulating layer to separate the conductive liquid from a metallic electrode to eliminate the problem of electrolysis,[18] which significantly broadens the potentials. Different aspects on electrowetting have been investigated. Welters *et al.*[19] and Sondag-Huethorst *et al.*[20] calculated the effective interfacial tension, which was reduced by an applied voltage. Berge[18] considered the minimization of the free energy and related the corresponding thermodynamic potentials by a Legendre transformation. Jones *et al.*[21,22] and Zeng *et al.*[23] investigated the forces exerted on a droplet and used the Maxwell stress tensor method for the calculation. Recent experiments revealed the saturation and instability of the contact angle when the applied voltage is above a critical value.[24–28] An intriguing phenomenon is that the contact line between a droplet and a substrate may lose stability under a relatively large field, leading to the ejection of small droplets from the edge of the mother droplet.[24,28] These experimental observations suggest that the electrowetting process involves rich dynamics. Capturing the physics requires a dynamic model beyond energetic analysis alone. Different from works focusing on equilibrium morphologies, in this paper we propose a phase field model that combines thermodynamics and viscous flow to predict the electrowetting process and the corresponding morphology evolution. In contrast to sharp interface, the phase field model exploits the concept of diffuse interface, which has been shown to be a powerful approach in many studies.[29–34] Our approach allows study and design of systems of complex droplet morphologies, patterned electrodes, and topographical surface patterns. With the understanding of the dynamic aspects, we aim to elucidate how instability occurs and how it leads to various morphologies.

II. DYNAMIC MODEL

Figure 1 shows a conductive droplet on a thin dielectric layer. Electric field is applied to the system by connecting one end of the power supply to the droplet while the other to

a)Electronic mail: weilu@umich.edu.

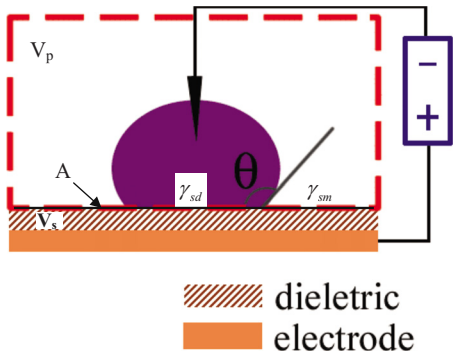

FIG. 1. (Color online) A schematic of a droplet on a dielectric substrate. An electric field is applied on the conductive droplet and the electrode beneath the dielectric layer. The region enclosed by the dashed line represents the phase field calculation domain. The contact angle is denoted by θ.

the electrode beneath the dielectric layer. We will use the phase field approach to model the morphological evolution of the droplet. In contrast to interface tracking methods such as boundary element methods, the interfaces are not modeled explicitly but given implicitly by the concentration field. Consequently, complex changes will not cause any additional computational difficulty. Phenomena such as a film breaking into isolated islands can be captured naturally. We have applied a similar approach to study interface diffusion problems in several material systems.[35–37] In the two-dimensional model in Fig. 1, we consider the region enclosed by the dashed line as a two-phase system composed of the droplet and the surrounding medium (air). Denote the concentration of each phase by its volume fraction, and define a spatially continuous and time dependent concentration function, $c(\mathbf{x},t)$, where $\mathbf{x}$ is the position vector and t is time. The droplet region is described by $c(\mathbf{x},t)=1$ while the medium by $c(\mathbf{x},t)=0$.

The free energy of the system depends on the phase configuration and electric field distribution, namely,

$$G=\int_{V_p}\left[f(c)+\frac{1}{2}h(\nabla c)^2-\frac{1}{2}\varepsilon_0\varepsilon_r(c)(\nabla\phi)^2\right]dV-\frac{1}{2}\int_{V_s}\varepsilon_0\varepsilon_r^s(\nabla\phi)^2dV+\int_A[\gamma_{sm}+(\gamma_{sd}-\gamma_{sm})\rho(c)]dA. \tag{1}$$

The first integration extends over the volume of the two-phase droplet and medium region, V_p. The second integration extends over the volume of the layer of the dielectric substrate, V_s. The last integration extends over the boundary area between the two volumes, A.

The first integration accounts for the energy in the two-phase region. The $f(c)$ term represents the chemical energy that drives phase separation. To describe phase separation, one may choose any function with double wells. Here we take $f(c)=f_0c^2(1-c)^2$, where f_0 is a positive constant. The function has two minima corresponding to the droplet and medium phases, respectively. The interfacial energy between the droplet and the medium is described by a concentration gradient term $h(\nabla c)^2$, where h is a material constant. The value of h can be related to surface tension.[38] The third term accounts for the electrostatic energy. Here, $\varepsilon_0=8.85\times10^{-12}$ F/m is the vacuum permittivity, ε_r is the dielectric constant, and ϕ is the electric potential. The dielectric constant may be interpolated using a transition function, $\rho(c)$, to make a rapid and smooth variation in the value, namely, $\varepsilon_r(c)=\varepsilon_r^{\text{droplet}}\rho(c)+\varepsilon_r^{\text{medium}}[1-\rho(c)]$. Here we take $\rho(c)=1/2[1-\tanh(5-10c)]$. Note that $\rho(c_{\text{droplet}})=1$ and $\rho(c_{\text{medium}})=0$. We will use the same $\rho(c)$ function for the surface integration part in Eq. (1). The specific form of $\rho(c)$ is insignificant when the interface is thin. We take $\varepsilon_r^{\text{droplet}}=0$ for the conductive droplet, which is an isopotential body with no electric field inside. Thus the corresponding volume integration of $\varepsilon_0\varepsilon_r(c)(\nabla\phi)^2/2$ in Eq. (1) vanishes inside the droplet.

The second integration accounts for the electrostatic energy in the dielectric substrate layer, where ε_r^s is the dielectric constant. The third integration describes the interfacial energy. Here γ_{sd} and γ_{sm} represent the interfacial energy per unit area between the substrate and the droplet, the substrate and the medium, respectively. The transition function, $\rho(c)$, effectively selects the corresponding boundary energy based on the phase variable c.

The system can change its configuration in two ways; mass relocation and electric field redistribution. The energy variation associated with mass relocation gives

$$\delta G=\int_{V_p}\left[f'(c)\delta c+h(\nabla c)\delta(\nabla c)-\frac{1}{2}\varepsilon_0\varepsilon_r'(c)\times(\nabla\phi)^2\delta c\right]dV+\int_A(\gamma_{sd}-\gamma_{sm})\rho'(c)\delta c dA. \tag{2}$$

Here $f'(c)=df(c)/dc$. The variation essentially defines a chemical potential $\mu=\delta G/\delta c$ which can be obtained by applying the divergence theorem to Eq. (2). By prescribing a boundary condition of $h\mathbf{n}\cdot\nabla c+(\gamma_{sd}-\gamma_{sm})\rho'(c)=0$ on area A to cancel the area integration, where $\mathbf{n}$ is the normal direction of A, we obtain

$$\mu=f'(c)-h\nabla^2c-1/2\varepsilon_0\varepsilon_r'(c)(\nabla\phi)^2. \tag{3}$$

When diffusion is the only mass transport mechanism, the mass flux is given by $\mathbf{J}=-M\nabla\mu$, where M is the mobility. A viscous flow with velocity $\mathbf{v}$ adds a convective term, $c\mathbf{v}$, to the flux, where $\mathbf{J}=-M\nabla\mu+c\mathbf{v}$. Here we consider an incompressible flow so that $\nabla\cdot\mathbf{v}=0$. The application of the mass conservation relation, $\partial c/\partial t+\nabla\cdot\mathbf{J}=0$, leads to a convective Cahn–Hilliard equation, namely,

$$\frac{\partial c}{\partial t}+\mathbf{v}\cdot\nabla c=\nabla(M\nabla\mu). \tag{4}$$

The droplet and medium cannot transport pass the boundary A, which leads to a boundary condition of $\mathbf{n}\cdot\mathbf{J}=0$. This condition can be written as $\mathbf{n}\cdot\nabla\mu=0$ since the flow velocity vanishes on the boundary A due to the nonslip boundary condition. To consider diffusion on the surface of the droplet, we take the form $M(c)=M_0c(1-c)$, where M_0 is a constant. Note that $M(c)$ vanishes outside the interfacial region.

With the presence of a diffuse interface, the equation describes the viscous flow of the liquid droplet is[39]

$$0 = -\nabla p + \nabla \cdot (\eta \nabla \mathbf{v}) + \mu \nabla c. \tag{5}$$

Here η is the viscosity, and p the pressure that enforces the incompressibility constraint $\nabla \cdot \mathbf{v} = 0$. The viscosity is dependent on the concentration, $\eta = \eta_0 c$, where η_0 is the droplet viscosity. The last term $\mu \nabla c$ accounts for the force at the interface. For a microscale droplet, the Reynolds number is small so that the inertial term has been neglected. Equations (4) and (5) need to be solved simultaneously to obtain evolution sequence of the system.

The electric potential satisfies the Laplace equation,

$$\nabla \cdot (\varepsilon_r \nabla \phi) = 0. \tag{6}$$

In the substrate region the dielectric constant in Eq. (6) is replaced by ε_r^s. Note that the substrate can significantly affect the evolution of the droplet by influencing the electric field distribution. The droplet is conductive and an isopotential body. The boundary of the droplet is obtained by the $c = 0.5$ contour. The electric field calculation domain includes the dielectric layer and the two phase region outside the droplet. We prescribe the Dirichlet boundary conditions on the surfaces of the droplet ($\phi = 0$) and the electrode ($\phi =$ applied voltage), and Neumann boundary conditions on other boundaries.

Normalize Eqs. (4)–(6) with a characteristic velocity V_c, length L_c, and time $t_c = L_c / V_c$. Equation (6) retains the same form after normalization. The choice of the magnitudes of the characteristic quantities depends on the physical details to resolve and computational convenience. The normalized equations are given by

$$\frac{\partial c}{\partial t} + \mathbf{v} \cdot \nabla c = \frac{1}{\mathrm{Pe}} \nabla \cdot (M \nabla \mu), \tag{7}$$

$$\mu = f'(c) - \mathrm{Ch}^2 \nabla^2 c - \frac{1}{2} \varepsilon_r'(c) (\nabla \phi)^2, \tag{8}$$

$$-\nabla p + \nabla \cdot (\eta \nabla \mathbf{v}) + \frac{1}{\mathrm{Ca}} \mu \nabla c = 0. \tag{9}$$

The mobility M and viscosity η are dimensionless numbers normalized by the mobility and viscosity of the droplet, M_0 and η_0. We have the normalized expression $f'(c) = (4c^3 - 6c^2 + 2c)$. The potential field ϕ is normalized by $\phi_c = L_c \sqrt{f_o / \varepsilon_0}$. The Péclet number, $\mathrm{Pe} = V_c L_c / (M_0 f_0)$ reflects the ratio of the diffusive time scale and the convective time scale. The significance of the interface energy is described by the Cahn number, $\mathrm{Ch} = \sqrt{h / f_0} / L_c$. Define $\beta = (\gamma_{sd} - \gamma_{sm}) L_c / h$. The normalized boundary conditions on A for Eq. (7) are given by $\mathbf{n} \cdot \nabla \mu = 0$ and $\mathbf{n} \cdot \nabla c + \beta \rho'(c) = 0$. The capillary number $\mathrm{Ca} = \eta_0 V_c / (L_c f_0)$ affects the relative magnitude of viscous force and interface force. Non-slip boundary condition on A is applied for Eq. (9).

III. NUMERICAL APPROACH

We first develop a finite element approach to solve the diffusion Eqs. (7) and (8). Following the standard procedure for variational formulation,[40,41] we take a weighted integral of the governing equation with a test function $w(\mathbf{x})$. After integration by parts, the problem becomes finding a function of c such that

$$\left(\frac{\partial c}{\partial t}, w \right)_{V_p} + (\mathbf{v} \cdot \nabla c, w)_{V_p} + \left(\frac{M}{\mathrm{Pe}} \nabla \mu, \nabla w \right)_{V_p} = 0, \tag{10}$$

$$(\mu, w)_{V_p} = (f', w)_{V_p} + \mathrm{Ch}^2 (\nabla c, \nabla w)_{V_p} - \frac{1}{2} (\varepsilon_r' (\nabla \phi)^2, w)_{V_p} + \mathrm{Ch}^2 (\beta \rho', w)_A. \tag{11}$$

Here the usually inner product notations, $(f, w)_{V_p} = \int_{V_p} f w dV$ and $(f, w)_A = \int_A f w dA$ are used. Note that substituting Eq. (8) into Eq. (7) directly would result in a fourth order derivative in c. This would require higher order continuity in the functions, and increase the computational complexity. We adopt a technique similar to what has been used in thin plate finite element by considering Eqs. (7) and (8) separately. Two separate forms, Eqs. (10) and (11), are obtained. This technique strategically avoids directly formulating a fourth order derivative in the diffusion equation.

A function such as $c(\mathbf{x}, t)$ can be expressed by interpolating shape functions $N_j(\mathbf{x})$ and the nodal values,

$$c(\mathbf{x}, t) = \sum_j N_j(\mathbf{x}) c_j(t). \tag{12}$$

Here c_j is the nodal value of c at node point j of the element. Similarly, we have $w(\mathbf{x}, t) = \Sigma_j N_j(\mathbf{x}) c_j(t)$ and $\mu(\mathbf{x}, t) = \Sigma_j N_j(\mathbf{x}) \mu_j(t)$. Putting these expressions into Eq. (10), we obtain a system of ordinary differential equations in the form of

$$\mathbf{A}_1 \frac{d\mathbf{c}(t)}{dt} + \mathbf{A}_2 \mathbf{c}(t) = \mathbf{a}(t), \tag{13}$$

where $\mathbf{c} = (c_1, c_2, \ldots)^T$, $[\mathbf{A}_1]_{ij} = \int N_i N_j dV$, $[\mathbf{A}_2]_{ij} = \int N_i (\mathbf{v} \cdot \nabla N_j) dV$, and $[\mathbf{a}]_i = -\int (M / \mathrm{Pe}) \nabla \mu \cdot \nabla N_i dV$.

We partition the time domain $0 \le t \le T$ into equal intervals of time step Δt. At $t = 0$, the solution is known from the initial configuration. To advance the solution in time from step n to $n+1$, we use the forward Euler algorithm, $d\mathbf{c}^n / dt = (\mathbf{c}^{n+1} - \mathbf{c}^n) / \Delta t$, where $\mathbf{c}^n = \mathbf{c}(n \Delta t)$. Then Eq. (13) is discretized as

$$\mathbf{c}^{n+1} = \Delta t \mathbf{A}_1^{-1} [\mathbf{a}^n - \mathbf{A}_2 \mathbf{c}^n] + c^n, \tag{14}$$

where $\mathbf{a}^n = \mathbf{a}(n \Delta t)$.

Following the similar procedure, we can obtain the discrete form of Eq. (11), where

$$\mathbf{B} \boldsymbol{\mu}(t) = \mathbf{b}_1 + \mathbf{b}_2 + \mathbf{b}_3 + \mathbf{b}_4, \tag{15}$$

where $\boldsymbol{\mu} = (\mu_1, \mu_2, \ldots)^T$, $[\mathbf{B}]_{ij} = \int N_i N_j dV$, $[\mathbf{b}_1]_i = \int (4c^3 - 6c^2 + 2c) N_i dV$, $[\mathbf{b}_2]_i = \mathrm{Ch}^2 \int \nabla c \cdot \nabla N_i dV$, $[\mathbf{b}_3]_i = -(1/2) \int \varepsilon_r' (\nabla \phi)^2 N_i dV$, and $[\mathbf{b}_4]_i = \mathrm{Ch}^i \beta \int \rho' N_i dA$.

We use the regular finite element approach to solve the electric potential field Eq. (6) and the flow field Eq. (9). The term $\mu \nabla c / \mathrm{Ca}$ in Eq. (9) is treated as a body force. It is a natural choice to calculate diffusion, flow and electric field on the same finite element mesh for coupling. The following is the outline to compute $\mathbf{c}^{n+1}$ from $\mathbf{c}^n$. First, compute the

electric field φ^n at the nodal points that corresponds to the concentration distribution $\mathbf{c}^n$. Then substitute the solution of φ^n into the Eq. (15) to get $\boldsymbol{\mu}^n$, and the modified Navier–Stokes equation to get $\mathbf{v}^n$. Substituting $\boldsymbol{\mu}^n$ and $\mathbf{v}^n$ into Eq. (14) gives $\mathbf{c}^{n+1}$. Repeat the procedure to evolve the concentration profile and thus the droplet morphology.

IV. RESULTS AND DISCUSSIONS

In the phase field model, the interface thickness is given by $\delta=\sqrt{h/W}$, where W is the barrier height between the two wells in the free energy function f.[38] In our model the value of W is $f_0/16$. The relation between the surface energy and phase field parameters can be obtained by interface profile integration. When two phases corresponding to the two wells of f are in equilibrium with a flat interface, the concentration profile takes the form of $c=1/2[1+\tanh(4x/\delta)]$. Then the surface energy density between the droplet and the medium, γ_{dm}, can be calculated from

$$\gamma_{dm}=\int_{-\infty}^{\infty}h\left(\frac{\partial c}{\partial x}\right)^2dx=\frac{1}{3}\sqrt{hf_0}. \tag{16}$$

When the medium is air, γ_{dm} is the surface energy of the droplet.

We take $\sqrt{h/f_0}=1$ nm, which gives an interface thickness of about 4 nm. This is sufficient to capture the interface location well. The surface energy of a water droplet in the air is 0.07 J/m^2. From the relationship in Eq. (16) we have $f_0=2.1\times10^8$ J/m^3 and $h=2.1\times10^{-10}$ J/m. Take $L_c=10$ nm to scale the phenomena we are interested in. The corresponding Cahn number is 0.1. The characteristic time $t_c=L_c/V_c$ is the time required for the fluid to be convected a distance on the order of the characteristic length, $t_c\sim0.1$ μs. The viscosity of water at room temperature is about 10^{-3} Pa s. The corresponding capillary number, Ca, is about 4.76×10^{-5}. To relate M_0 to an experimentally accessible quantity, one may linearize Eqs. (7) and (8) around the equilibrium concentration.[42] This gives a common diffusion equation with the corresponding diffusion coefficient being $D=2M_0f_0$. The diffusion coefficient of water at room temperature is about 0.2272 Å^2/ps. These values give Pe$\sim$0.88.

All the simulations are performed on a rectangular two-phase domain with dimensions of 560×320 in length normalized by L_c. The initial configuration is a circular droplet with radius of 80 in contact with the substrate surface. The dielectric substrate has $\varepsilon_r^s=4$ with a thickness of 5. We choose the calculation domain size to be large enough so that it provides enough space for the morphological evolution of the droplet. We first calculate the contact angle without electric field. The parameter β indicates the substrate/medium and substrate/droplet interfacial energy difference, which affects the contact angle. The simulations start with a circular droplet just in contact with the substrate, which has an initial contact angle close to 180°. We find that the contact angle changes faster comparing to the overall morphology evolution since changing the contact angle only involves a small amount of local mass transport around the edge of the droplet. We measure the equilibrium contact angle from the simulation and compare them with the analytical results. The measurement is achieved by using the 0.5 contour to obtain the droplet morphology, and then calculating the slope near the contact region. The analytical equilibrium angle is obtained from the Young's relation, $\cos\theta_c=(\gamma_{sm}-\gamma_{sd})/\gamma_{dm}$. Consider the parameter $\beta=(\gamma_{sd}-\gamma_{sm})L_c/h$. A hydrophilic surface has $\beta<0$ where the droplet/substrate interface has lower energy and the droplet wets the substrate. This leads to an equilibrium contact angle θ_c less than 90°. On the other hand, a hydrophobic surface has $\beta>0$ and an equilibrium contact angle θ_c greater than 90°. With $L_c=10$ nm, $h=2.1\times10^{-10}$ J/m, and $\gamma_{dm}=0.07$ J/m^2, we have $\cos\theta_c=-0.3\beta$. This relation is represented by the straight line in Fig. 2. The simulation results agree well with the theoretical predictions.

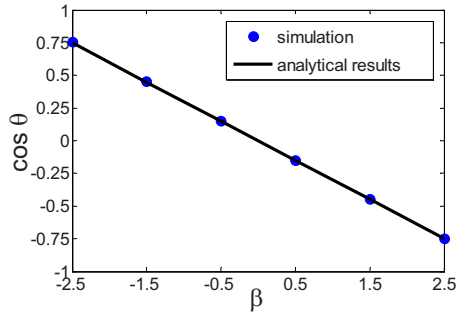

FIG. 2. (Color online) The equilibrium contact angles from simulations agree well with the analytical results of the Young's relation, $\cos\theta_c=-0.3\beta$.

Figure 3 shows representative results of the droplet morphology evolution when an electric field is applied. The simulations start from the equilibrium morphology without an electric field. Results for various applied electric potential are given. In all simulations β is taken to be -0.5. A higher applied voltage leads to larger driving force and thus faster morphology evolution. The droplet becomes more wetting with increased voltage, which is indicated by the decreased contact angle in column c. Our simulations show that when the voltage is low and the dielectric layer is thin, the equilibrium contact angle under electric field, θ, follows $(\cos\theta-\cos\theta_c)\sim\phi^2$. This relation is consistent with the Lippmann–Young law.[43] Some recent analyses suggest that

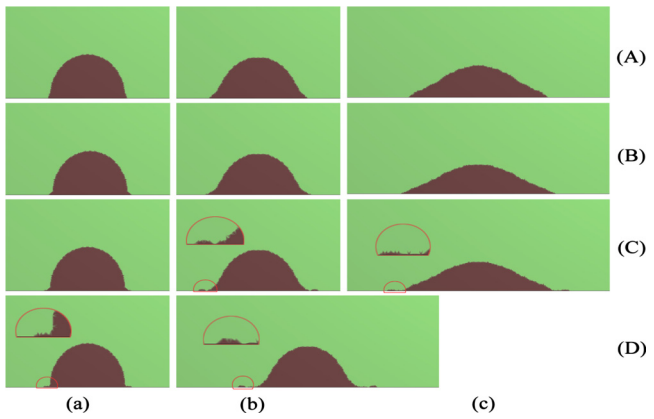

FIG. 3. (Color online) Morphology evolution of droplets under various applied voltages. Each row corresponds to an evolution sequence under an applied voltage. A: $\phi=0.6$, B: $\phi=0.8$, C: $\phi=1.0$, D: $\phi=1.2$. a: $t=20$, b: $t=200$, and c: $t=600$. The parameter β is taken to be -0.5.

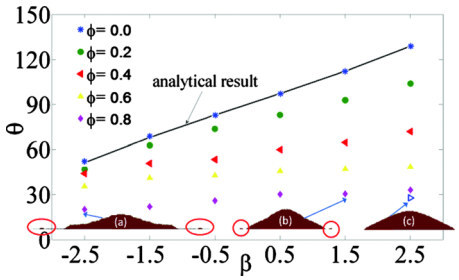

FIG. 4. (Color online) Effect of electric voltage on the contact angle and stability.

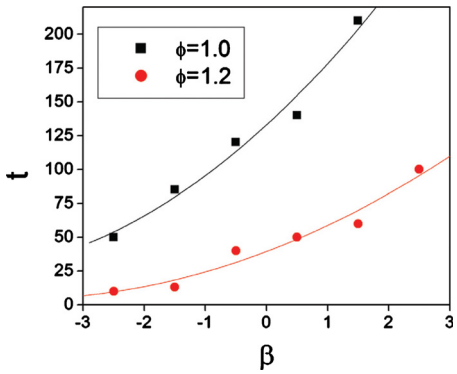

FIG. 5. (Color online) Evolution time from the initial equilibrium morphology to the emergence of instability.

the surface profiles of droplets may display a diverging curvature at local regions very close to the contact line.[44–46] We do not aim to resolve such very local effect in this study, which requires extremely fine mesh. When the applied voltage is high enough, as shown in row C, ripples starts to emerge at the droplet edges at about $t=200$. This instability is qualitatively consistent with recent experimental observations,[24,28] where the contact line has been found to become unstable at a high voltage, leading to the ejection of small droplets from the edge of the original droplet. With a higher voltage in row D, the instability appears earlier at about $t=20$, when the overall droplet morphology has not evolved much.

Our simulations suggest that instability happens by first forming an extruding layer at the edge of the droplet. This initially continuous thin layer breaks into small droplets during its extension. To understand this breakage mechanism, it is illuminating to imagine a thin liquid film under an electric field, e.g., the field in the fringe of a droplet. The surface energy prefers a flat surface while the electric static energy prefers a wavy surface. The competition determines a fast growth wavelength of the surface perturbation. The electrostatic energy per volume is proportional to $\varepsilon_0 V^2$ while the surface energy per area is proportional to γ_{dm}. Thus the wavelength is proportional to $\gamma_{dm}/\varepsilon_0 V^2$. For a given instability mode or wavelength, larger droplet surface energy requires higher instability voltage. While detailed morphology evolution has been obtained from our numerical simulations, this simple picture may help to explain the experimental observation that droplet ejection can be suppressed by adding salt to the water droplet. The ion–dipole bond formed between the water molecule and ion is stronger than the hydrogen bond formed between the water molecules. The additional energy needed to break the stronger bond raises the surface energy. It is this increase in surface energy that contributes to suppress the instability.

We have conducted a parametric study to investigate how β affects the instability and summarized the results in Fig. 4. For each given β, the measured contact angle decreases with voltage. For each given voltage, the contact angle increases with β. When the voltage is high enough, say $\phi=1$, droplets with smaller β starts to lose stability. Insets (a) with $\beta=-2.5$ and (b) with $\beta=1.5$ show the morphology and instability. Small isolated droplets with similar dimensions emerge at the edge of the original droplets in both situations. The droplet with lower β demonstrates lower profile and more contact area with the substrate. However, a droplet with higher β can be stable under the same applied voltage. The inset (c) shows an example of a stable morphology for $\beta=2.5$. Our simulations show that the emergence of instability involves a decrease of the contact angle first. For hydrophobic surface with $\theta>90°$, an applied high voltage will first cause the contact angle to become less then 90°, followed by the extrusion of a thin layer from the edge of the droplet, and further breakage into small droplets. Figure 5 shows the time it takes from the initial equilibrium morphology to the emergence of instability after an electric field is applied. It can be observed that instability emerges more quickly for small β or small initial equilibrium contact angles. Instability also emerges more quickly under larger electric fields.

In summary, our model and simulations have revealed the morphology evolution of a droplet on a dielectric substrate and the essential dynamic process about how instability emerges. The onset of the emission of small droplets is related to the competition between the smoothing effect of the surface energy and the roughing effect of the electrostatic energy. Thus by changing parameters, such as the surface energy of the droplet, the instability can be suppressed. The proposed modeling and simulation approaches can provide useful guidance for designing novel micro/nanoscale devices where electrowetting mechanism is used to dynamically change the morphology.

ACKNOWLEDGMENTS

The authors acknowledge financial support from National Science Foundation Award No. CMMI-0700048 and support from National Natural Science Foundation of China (10972121 and 10810401006).

[1]F. Vinet, P. Chaton, and F. Fouillet, Microelectron. Eng. **41**, 61 (2002).
[2]P. Gwynne and G. Heebner, Science **298**, 625 (2002).
[3]T. H. Chen, Y. J. Chuang, C. C. Chieng, and F. G. Tseng, J. Micromech. Microeng. **17**, 489 (2007).
[4]A. Klingner and F. Mugele, J. Appl. Phys. **95**, 2918 (2004).
[5]S. Kuiper and B. H. W. Hendriks, Appl. Phys. Lett. **85**, 1128 (2004).
[6]B. Berge and J. Peseux, Eur. Phys. J. E **3**, 159 (2000).
[7]S. Yang, T. N. Krupenkin, P. Mach, and E. Chandross, Adv. Mater. (Weinheim, Ger.) **15**, 940 (2003).
[8]R. A. Hayes and B. J. Feenstra, Nature (London) **425**, 383 (2003).
[9]Z. Q. Lin, T. Kerle, S. M. Baker, D. A. Hoagland, E. Schaffer, U. Steiner, and T. P. Russell, J. Chem. Phys. **114**, 2377 (2001).
[10]Z. Q. Lin, T. Kerle, T. P. Russell, E. Schaffer, and U. Steiner, Macromol-

ecules **35**, 3971 (2002).
[11]D. Merkt, A. Pototsky, M. Bestehorn, and U. Thiele, Phys. Fluids **17**, 064104 (2005).
[12]R. Verma, A. Sharma, K. Kargupta, and J. Bhaumik, Langmuir **21**, 3710 (2005).
[13]D. Bandyopadhyay and A. Sharma, J. Colloid Interface Sci. **311**, 595 (2007).
[14]K. John, P. Hanggi, and U. Thiele, Soft Matter **4**, 1183 (2008).
[15]K. John and U. Thiele, Appl. Phys. Lett. **90**, 264102 (2007).
[16]J. R. Melcher and G. I. Taylor, Annu. Rev. Fluid Mech. **1**, 111 (1969).
[17]G. Lippmann, Ann. Chim. Phys. **5**, 494 (1875).
[18]B. Berge, C. R. Acad. Sci. Ser. II **317**, 157 (1993).
[19]W. J. J. Welters and L. G. Fokkink, Langmuir **14**, 1535 (1998).
[20]J. A. M. Sondag-Huethorst and L. G. Fokkink, Langmuir **10**, 4380 (1994).
[21]T. B. Jones, Langmuir **18**, 4437 (2002).
[22]T. B. Jones, J. D. Fowler, Y. S. Chang, and C. J. Kim, Langmuir **19**, 7646 (2003).
[23]J. Zeng and T. Korsmeyer, Lab Chip **4**, 265 (2004).
[24]M. Vallet, M. Vallade, and B. Berge, Eur. Phys. J. B **11**, 583 (1999).
[25]H. J. J. Verheijen and M. W. J. Prins, Langmuir **15**, 6616 (1999).
[26]B. Shapiro, H. Moon, R. L. Garrel, and C. J. Kim, J. Appl. Phys. **93**, 5794 (2003).
[27]V. Peykov, A. Quinn, and J. Ralston, Colloid Polym. Sci. **278**, 789 (2000).
[28]F. Mugele and S. Herminghaus, Appl. Phys. Lett. **81**, 2303 (2002).
[29]D. M. Anderson, G. B. McFadden, and A. A. Wheeler, Annu. Rev. Fluid Mech. **30**, 139 (1998).
[30]D. Jasnow and J. Vinals, Phys. Fluids **8**, 660 (1996).
[31]R. Borcia and M. Bestehorn, Phys. Rev. E **67**, 066307 (2003).
[32]S. Madruga and U. Thiele, Phys. Fluids **21**, 062104 (2009).
[33]U. Thiele, S. Madruga, and L. Frastia, Phys. Fluids **19**, 122106 (2007).
[34]H. W. Lu, K. Glasner, A. L. Bertozzi, and C. J. Kim, J. Fluid Mech. **590**, 411 (2007).
[35]D. Kim and W. Lu, J. Mech. Phys. Solids **54**, 2554 (2006).
[36]W. Lu and D. Salac, Phys. Rev. Lett. **94**, 146103 (2005).
[37]W. Lu and Z. Suo, J. Mech. Phys. Solids **49**, 1937 (2001).
[38]J. W. Cahn and J. E. Hilliard, J. Chem. Phys. **28**, 258 (1958).
[39]M. E. Gurtin, D. Polignone, and J. Viñals, Math. Models Meth. Appl. Sci. **6**, 815 (1996).
[40]T. Hughes, *The Finite Element Method: Linear Static and Dynamic Finite Element Analysis* (Dover, Elk Grove Village, IL, 2000).
[41]B. Sun, Z. Suo, and W. Yang, Acta Mater. **45**, 1907 (1997).
[42]T. Roths, C. Friedrich, M. Marth, and J. Honerkamp, Rheol. Acta **41**, 211 (2002).
[43]C. Quilliet and B. Berge, Curr. Opin. Colloid Interface Sci. **6**, 34 (2001).
[44]J. Buehrle, S. Herminghaus, and F. Mugele, Phys. Rev. Lett. **91**, 086101 (2003).
[45]F. Mugele and J. Buehrle, J. Phys.: Condens. Matter **19**, 375112 (2007).
[46]A. G. Papathanasiou and A. G. Boudouvis, Appl. Phys. Lett. **86**, 164102 (2005).